Effects of MgO Nanoparticle Additions on the Structure and Mechanical Properties of Continuously Cast Steel Billets

XIANGZHOU GAO, SHUFENG YANG, JINGSHE LI, YINDONG YANG, KINNOR CHATTOPADHYAY, and ALEX MCLEAN

A new approach for pre-dispersing MgO nanoparticles and adding them to molten steel during continuous casting operations was established. The influence of different mass fractions of MgO nanoparticles on inclusion characteristics, steel microstructure, and the ability of inclusions to induce acicular ferrite (AF) formation, was investigated. The results revealed that after adding different mass fractions of nanoparticles, the majority of inclusions contained $MgO\text{-}Al_2O_3$, and the inclusion size was considerably refined. These inclusions promoted AF formation, and with increasing inclusion size from 1.0 to 1.8 μm, the proportion of AF progressively increased. The ability of inclusions to induce AF was greatly reduced when the inclusion size reached 7.0 μm. This was primarily due to the relationship between the ferrite nucleation rate and inclusion size. It was also found that the size of inclusions that functioned as pinning particles was larger than that of inclusions that served as AF nucleation cores. When the mass fraction of MgO nanoparticles reached 0.05 pct, the degree of interlocking of AF within the microstructure of billet specimens was maximized and this was associated with optimal values for strength and impact properties.

DOI: 10.1007/s11661-015-3237-1
© The Minerals, Metals & Materials Society and ASM International 2015

I. INTRODUCTION

DURING recent years, there have been increasing efforts[1–5] to develop steel materials with improved mechanical properties to meet the strong demand from many heavy industries. It is well known that refining of the steel microstructure can significantly improve mechanical properties, particularly strength, plasticity, and toughness. The refining methods generally involve retarding austenite grain growth and developing fine acicular ferrite structure, thus improving the mechanical properties primarily through impeding dislocation movement within the microstructure when external forces are applied. To obtain appropriate microstructures, precipitation strengthening and thermo-mechanical processing are the most common methods.[6,7] Generally, the latter can be achieved during actual production through austenite non-recrystallization controlled rolling,[8] strain-induced transformation, and accelerated cooling.[9,10] However, the precise control of important parameters such as micro-alloy content, cooling, and rolling conditions must be specifically investigated in order to satisfy the individual requirements of different steels, all of which increases the complexity of process control. The precipitation strengthening method was first proposed by Zener[11] in 1949. This involves incorporating micro second phase particles in the steel to retard the growth of austenite grain and induce intragranular acicular ferrite (IAF) as the nucleation cores of ferrites. These second phase particles can be generated either by an internal precipitation method (IPM) or by an external addition method (EAM).

Hitherto, the majority of researchers have focused on an IPM to obtain small-sized, thermally stable, second phases, generally less than or equal to 1 μm,[12] through adjusting steel chemistry and steelmaking conditions. This refinement mechanism is basically consistent with "oxide metallurgy" theory.[13,14] Many experiments have been performed to study the ability of titanium oxides to promote the formation of AF and it has been concluded that Ti_2O_3 is superior to other species in this regard.[15–20] Additional studies[21–23] indicate that inclusions such as zirconium oxides, titanium, niobium and vanadium carbonitrides, cerium sulfides, and high-melting titanium nitride also serve as heterogeneous nuclei for fine ferrite. To obtain appropriate steelmaking conditions, the precipitation temperature of the required particles needs to be decreased and this demands higher purity of the steel melt as well as a controlled casting process.[24]

XIANGZHOU GAO, Ph.D. Candidate, SHUFENG YANG, Associate Professor, and JINGSHE LI, Professor, are with the State Key Laboratory of Advanced Metallurgy, University of Science and Technology Beijing, Beijing, 100083, P.R. China, and also with the School of Metallurgical and Ecological Engineering, University of Science and Technology Beijing. Contact e-mail: yangshufeng@ustb.edu.cn YINDONG YANG, Senior Research Associate, KINNOR CHATTOPADHYAY, Assistant Professor, and ALEX MCLEAN, Professor Emeritus, are with the Department of Materials Science and Engineering, University of Toronto, Toronto, ON, M5S 3E4, Canada.
Manuscript submitted August 8, 2015.
Article published online November 12, 2015

EAM was first proposed in 1978 when Hasegawa *et al.*[25] developed a new technique based on the Spray-Dispersion Method[26–28] to produce a steel containing homogeneously dispersed fine ZrO_2 and Al_2O_3 particles which were sprayed into the molten steel. This research was performed using a high-frequency induction furnace for an industrial test, and it was concluded that mechanical properties including hardness, proof strength and tensile strength, increased with the volume fraction of oxide particles. Gregg *et al.*[29] also established a method for the direct addition of titanium oxide particles into a steel melt using a high-frequency induction furnace and produced steel samples with controlled contents of powdered mineral phases. Other researchers[30,31] have carried out similar studies. In contrast with IPM, EAM has no excessive requirements for steel melt purity and is easier to control. Moreover, by adding particles externally, they not only have an effective influence on primary austenite grain behavior, but they also have beneficial effects during the subsequent rolling and heat treatment processes. For these reasons, EAM has several advantages compared with IPM. However, reports related to EAM, and particularly its application in actual production processes, are limited and problems remain pertaining to experimental design.

In the present study, an innovative pre-dispersion approach for the addition of nanoparticles into a steel melt during industrial operations is described. HPB300 steel was selected for test purposes. The chemical composition of the steel is shown in Table I. Magnesium oxide (MgO) nanoparticles were selected as the second phase species because of the relatively weak affinity between individual particles, minor lattice misfit with ferrite, and other appropriate characteristics.[32] The focus of this study involved investigation of the following aspects: (i) the influence of the amount of added MgO nanoparticles on inclusion characteristics, such as composition, morphology, and size; (ii) the influence of different mass fractions of MgO nanoparticles on the microstructure of continuously cast billet, and in particular on the ability of inclusions to induce the formation of AF; and (iii) the influence of different mass fractions of MgO nanoparticles on mechanical properties of the continuously cast billet.

II. PLANT TRIALS

A. *Materials Preparation*

To ensure that the MgO nanoparticles (15 to 25 nm) were well dispersed before adding to the steel melt, another nanoparticle material, AlSi alloy (50 to 70 nm, Al-70 wt pct, Si-30 wt pct), was used as the pre-dispersion medium. Due to the fact that aluminum and silicon are the most common deoxidant elements used in steelmaking, their addition would not cause contamination of the steel melt.

The pre-dispersion process of MgO nanoparticles was performed using a nano dispersing machine (IKN Mechanical Equipment Co., Ltd, Germany) with a weight ratio of MgO and AlSi alloy of 1:11. The rotation speed was maintained at 6000 rpm during the 3 hours process which was conducted under low oxygen and low temperature conditions to avoid the risk of high temperatures arising from particle collisions. Cast iron pipes, 1500 mm in length, outer diameter 11 mm, and wall thickness 1 mm, were used as carriers for up to 150 g of the mixed nanoparticles. The ends of the pipes were sealed with wooden plugs as shown in Figure 1. Figure 2 shows the micromorphology of mixed nanoparticles after compaction. The white areas indicated by arrows are MgO nanoparticles which have undergone slight agglomeration. However, the average size of the agglomerates is still less than 1 μm, a necessary premise for MgO nanoparticles' dispersion after addition to the steel melt.

B. *Plant Trials*

The longer the residence time of MgO nanoparticles in the steel melt, the greater the probability of collision and float-out. The higher the stirring intensity of the steel melt in the area where nanoparticles are added, the better the dispersion effect of the additive. With these considerations in mind, the vicinity of the submerged nozzle outlet was chosen as the addition location. In this region of the casting mold, there is relatively strong stirring of the steel and a relatively short distance to the end of billet solidification. Electromagnetic stirring in

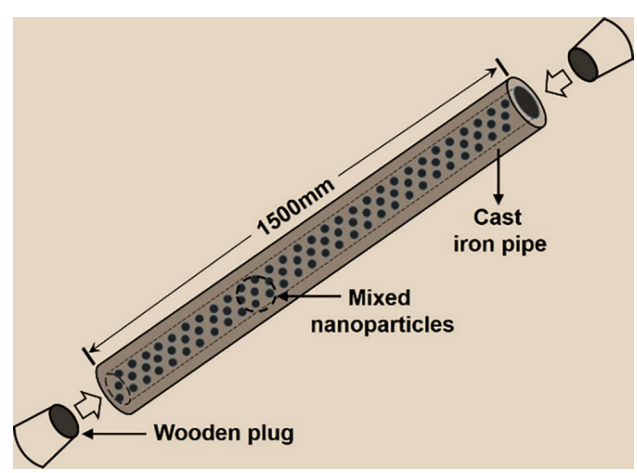

Fig. 1—Schematic diagram of a cast iron pipe filled with compacted nanoparticles.

Table I. Chemical Composition of the Test Steel (Weight Percent)

C	Si	Mn	P	S	Fe
0.20	0.14	0.45	0.023	0.023	bal.

this region could also further contribute to the dispersion of nanoparticles.

During this investigation, four different mass fractions of MgO nanoparticles, 0.01, 0.03, 0.05, and 0.07 pct, were evaluated during the industrial trial. The different mass fractions of MgO nanoparticles were distributed within four sections of billets during the continuous casting process. The mass fraction of MgO nanoparticles in any one section of billet was controlled by the addition speed of the cast iron pipes with the aid of a thread feeding machine located nearby the mold on the continuous casting platform. The casting speed was maintained constant at 2 m min^{-1}, and the length and weight of each billet were 9 m and 1.5 t, respectively. To ensure the MgO nanoparticles were distributed homogeneously within the billets, the feeding speed of the pipes was maintained at a constant value for each specific section of billet. Table II shows the addition strategy. Selecting the case for the highest mass fraction addition of nanoparticles, 0.07 pct, the addition to the molten steel of carbon from the cast iron pipes and aluminum and silicon from the AlSi nanoparticle alloy, would increase the C, Al, and Si contents of the steel by 0.0016, 0.0431, and 0.0185 pct, respectively. This would lower the liquidus temperature by less than half a degree. The aluminum and to a lesser extent the silicon will react with oxygen and participate in the formation of inclusions.

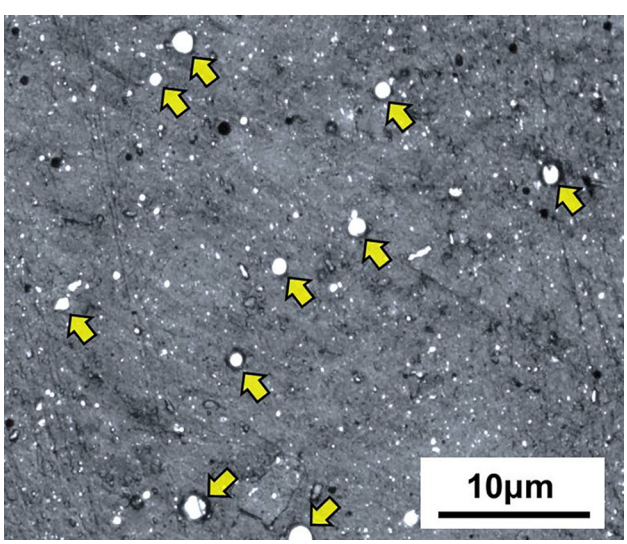

Fig. 2—Micromorphology of nanoparticles after compaction.

Throughout this paper, the benchmark steel, *i.e.*, steel without the addition of MgO nanoparticles, is defined as S0. Figure 3 shows a schematic diagram of the feeding and dispersion process of nanoparticles.

C. *Detection Methods*

1. *Inclusion detection*

Three cubic samples of 15 mm in side length were obtained every 2.5 m per section billet. After mechanical grinding and polishing, the samples were examined with scanning electron microscopy (SEM) and energy-dispersive spectrometry (EDS) to determine inclusion morphology, size, and type.

2. *Microstructure observation*

After etching the polished surface of steel samples with 4 pct nital for 15 seconds, the steel microstructure as well as the three-dimensional morphology of inclusions was examined with the aid of a metallographic microscope and the SEM.

3. *Mechanical properties*

The influence of different mass fractions of MgO nanoparticles on the steel microstructure is reflected by the change in mechanical properties. With this in mind, three standard test specimens for evaluating tensile strength, yield strength, and impact toughness were obtained from every 2.5 m per section billet.

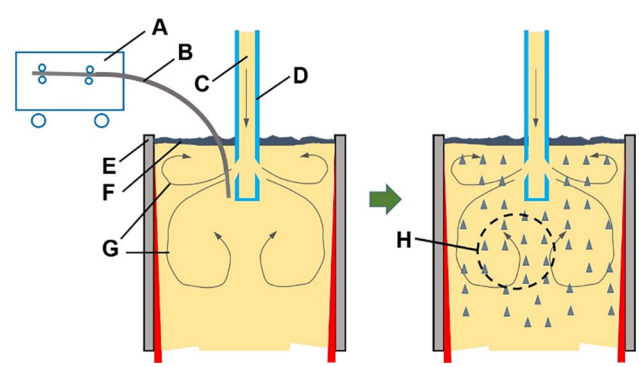

Fig. 3—Schematic diagram of nanoparticles addition and dispersion process. *A* Thread feeding machine; *B* Cast iron pipe (full of nanoparticles); *C* steel stream; *D* long nozzle; *E* mold; *F* mold powder; *G* steel liquid circulation; *H* dispersed nanoparticles.

Table II. Addition Scheme for Different Mass Fractions of MgO Nanoparticles

Plant Trial Group	Mass Fraction of MgO Nanoparticles (Pct)	Number of Added Cast Iron Pipes	Feeding Speed Per Cast Iron Pipe (mm min^{-1})
S1	0.01	1	330
S2	0.03	3	1000
S3	0.05	5	1660
S4	0.07	7	2330

III. RESULTS AND DISCUSSION

A. *Inclusion Characteristics*

The typical inclusion types in HPB300 steel without adding MgO nanoparticles are shown in Figure 4. MnS inclusions (gray fraction) always formed on the surface of SiO_2 or SiO_2-MnO inclusions (black fraction), which is in agreement with previous reports[33] that sulfide inclusions generally precipitate on the surface of oxide inclusions. In addition, there also existed many simple SiO_2-MnO hybrid inclusions. All of these inclusions were globular in shape and the average size was about 7 μm.

After adding MgO nanoparticles to the steel, the main inclusion type changed to MgO-Al_2O_3-MnO-MnS hybrid inclusions, and the morphology and average size of inclusions varied with different addition amounts of nanoparticles as shown in Figure 5. When the mass fraction of MgO nanoparticles was 0.01 or 0.03 pct, the common inclusions in steel were MgO-Al_2O_3-MnO-MnS hybrid inclusions, and the separation between sulfide and oxide was not obvious as illustrated in Figure 5(S1) and Figure 5(S2). When the mass fraction of MgO nanoparticles increased to 0.05 pct, in addition to the inclusions already mentioned, there appeared duplex inclusions consisting of MgO-Al_2O_3-MnO and either MnS or MgS-MnS as shown in Figure 5(S3). With increasing mass fraction of MgO nanoparticles to 0.07 pct, the proportion of duplex inclusions increased, Figure 5(S4). The morphologies of these inclusions were either globular or irregular.

The compositional change of inclusions as a function of MgO addition and its impact on inclusion morphology is shown in Figure 6. Based on this information, it can be concluded that the oxide particles consist mainly of MgO-Al_2O_3-MnO and the sulfide phase, MnS-MgS. With increase in amount of added MgO nanoparticles, the weight percentage of sulfide has an increasing trend that mainly relates to the size of the oxide inclusions. When low levels of MgO nanoparticles are added, for example, 0.01 or 0.03 wt pct, the oxide inclusions formed can be well dispersed under the strong stirring effect in the mold and the inclusion size is relatively small. This means that MnS and MgS can precipitate on the surface of a mass of oxide inclusions and also be well dispersed. The percentage of sulfide phase in the hybrid inclusions is small, and the size of the hybrid inclusions is also small. This makes it difficult to distinguish the duplex nature of the inclusions. However, when the addition amounts of MgO nanoparticles increase to 0.05 or 0.07 wt pct, the increased density of nanoparticles in the melt leads to increased probability of collision between adjacent particles. This results in a decrease in the number of oxide inclusions, while the inclusion size becomes larger, which makes observation of the morphological structure much easier. Since the total content of S and Mn in the melt is constant, the same amount of sulfide forms on fewer oxide inclusions, which ultimately leads to an increase in weight percentage of sulfide product with increasing amount of added nanoparticles.

With increasing amounts of MgO addition from 0.01 to 0.07 wt pct, the average size of inclusions gradually increased from 1.0, to 3.5 μm in samples S1 to S4, respectively. Compared to the average inclusion size of 7.0 μm in the initial sample S0, the results shown in Figure 7 indicate that the average size of inclusions was decreased by 85.7, 82.9, 74.3, and 50.0 pct, respectively.

B. *Microstructural Characteristics*

Figure 8 shows the microstructural evolution of billet samples with increasing mass fractions of MgO nanoparticles. In the S0 sample, the microstructure consisted of coarse banded ferrite (BF) and polygonal ferrite (PF). With addition of 0.01 wt pct MgO nanoparticles, some fine AF appeared, distributed within the coarse PF which was still the primary microstructural feature (Figure 8(S1)). When the mass fraction of MgO nanoparticles increased to 0.03 pct, the proportion of fine AF also increased and the average size of the crystals decreased (Figure 8(S2)). With 0.05 wt pct MgO nanoparticles, fine AF became the primary constituent and other types of ferrites were rarely observed (Figure 8(S3)). The AF crystals grew in different directions and improved the degree of interlocking. This type of microstructure hinders dislocation movement and reinforces the mechanical properties of the steel. However, when the added MgO nanoparticles increased to 0.07 wt pct, in S4, large numbers of PF grains were generated and the proportion of AF declined compared with the S3 sample.

To further study the refinement mechanism of the microstructure, some regions refined by AF in samples with different mass fractions of MgO nanoparticles were

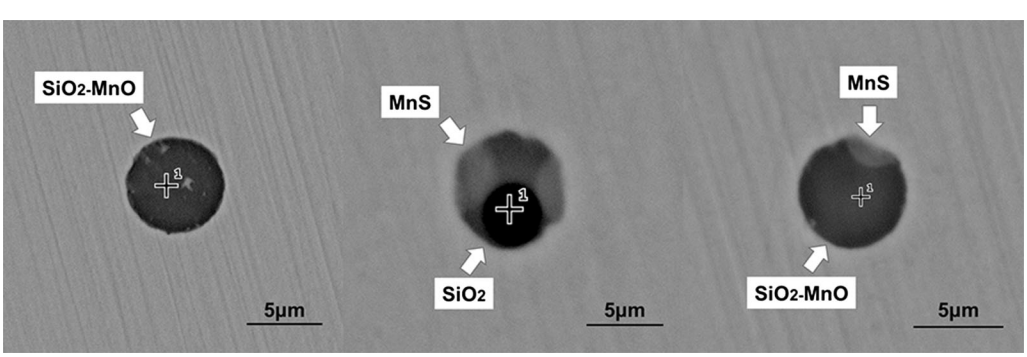

Fig. 4—Typical inclusion morphologies observed in steel S0.

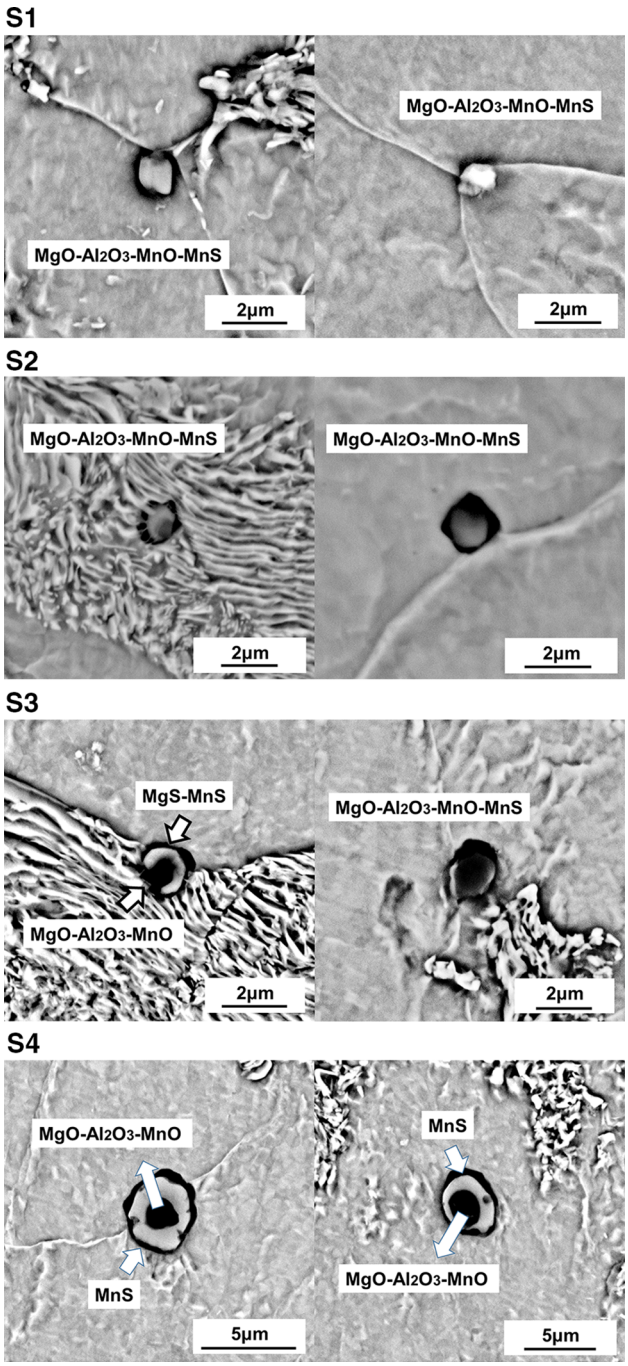

Fig. 5—Typical inclusion morphologies with different mass fractions of MgO nanoparticles.

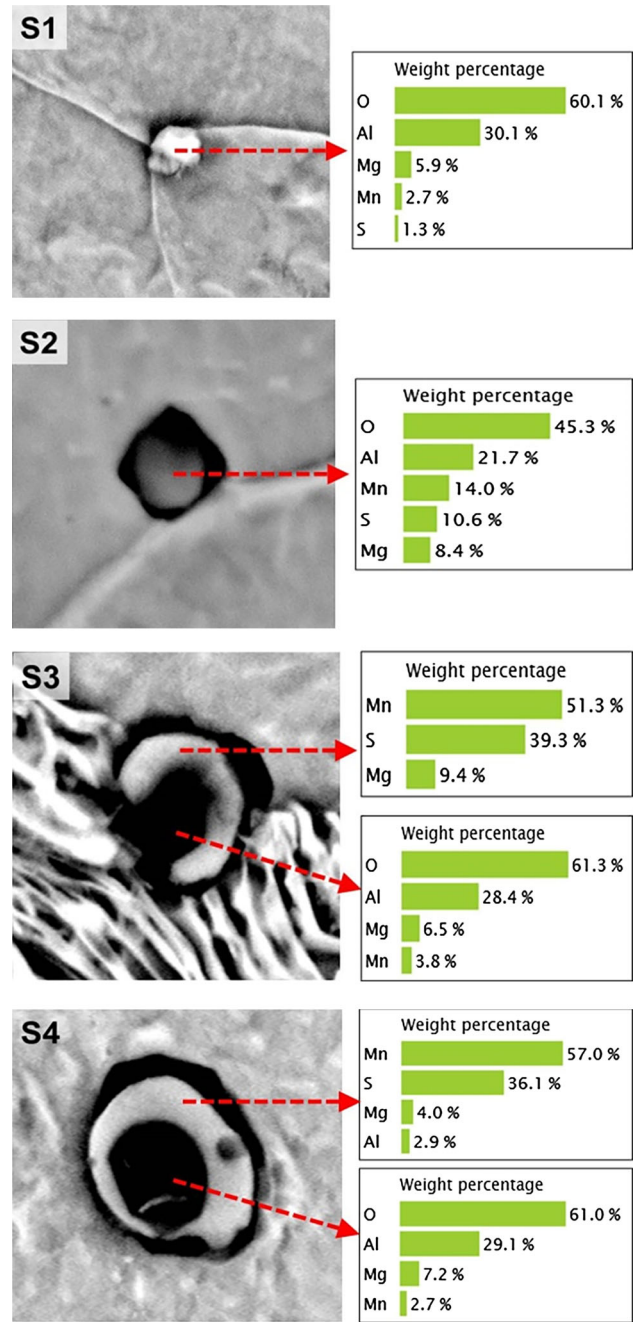

Fig. 6—Weight percentage of the constituent elements of typical inclusions.

examined using SEM. In these refined zones, there existed considerable IAF induced by inclusions as shown in Figure 9. These inclusions consisted of MgO-Al_2O_3-bearing constituents as illustrated in Figure 5. It was also observed that some inclusions were located on the PAGB as shown in Figure 10. Judging from the relationship between these inclusions and the growth direction of the primary austenite grains, it can be concluded that the inclusions acted as pinning particles to retard the growth of the austenite grains. In addition, the average size of these pinning particles was relatively larger than that of those inclusions inducing IAF. All of these observations were characteristic of the steel samples with different mass fractions of MgO nanoparticles.

C. *Mechanical Properties*

The variations of yield strength, tensile strength, and impact energy with increase in added amounts of MgO nanoparticles, are shown in Figure 11. All of the

mechanical property parameters increase to different degrees with different mass fractions of MgO nanoparticles. The variation of yield and tensile strengths with mass fraction shows a complex dependence. With the addition of 0.01 wt pct MgO nanoparticles, the yield strength does not show much change, while tensile strength shows significant increase. With higher mass fractions, the yield strength increases, while the increment in tensile strength is not so much. This inconsistent trend is contingency phenomena. Due to the restrictive conditions that influence the production process, the industrial trials were limited in duration. Considering the instability associated with the addition during the initial stage of the trials, it is quite possible that the nanoparticles distribute non-homogeneously within the billets, which ultimately leads to a relatively large error in values of mechanical properties. After the method of addition is stabilized, the uniform dispersion of nanoparticles is much better. This explains why the error values of yield strength and tensile strength decrease gradually with increasing mass fractions of MgO nanoparticles as shown in Figure 11(A). In general, the tensile strength of billet specimens was substantially improved compared with that in the absence of nanoparticle additions. The difference in strength values with different mass fractions of nanoparticles is however, relatively small, from about 45.1 to 53.0 pct with additions of 0.01–0.05 pct, respectively. Compared with the tensile strength, the variation in yield strength of billet specimens is significantly more dependent on the amount of added nanoparticles. With the increase in mass fraction of nanoparticles, the yield strength first increased and then decreased. The peak value occurred at 0.05 wt pct. Based on these findings, the optimal mass fraction is 0.05 pct as indicated by the red frame in Figure 11(A). Figure 11(B) shows the variation in impact energy of billet specimens containing different mass fractions of MgO nanoparticles at test temperatures of 253 K, 273 K, and 293 K (−20 °C, 0 °C, and 20 °C, normal room temperature). In all cases, the impact energy first increased to a maximum at the mass fraction of 0.05 pct as indicated by the red frame and then decreased. The highest value of impact energy occurred at room temperature and decreased with decreasing temperature. From analysis of these results, the optimal mass fraction of MgO nanoparticles is 0.05 pct.

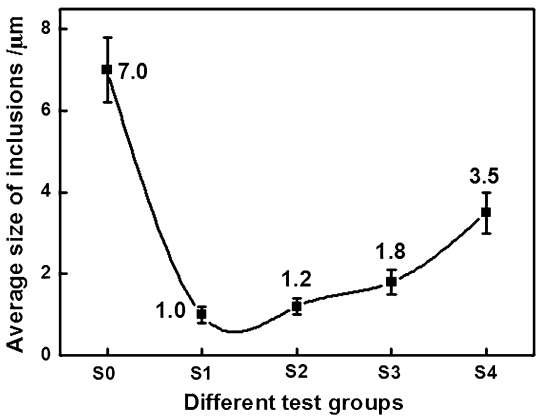

Fig. 7—Average inclusion size in different test groups.

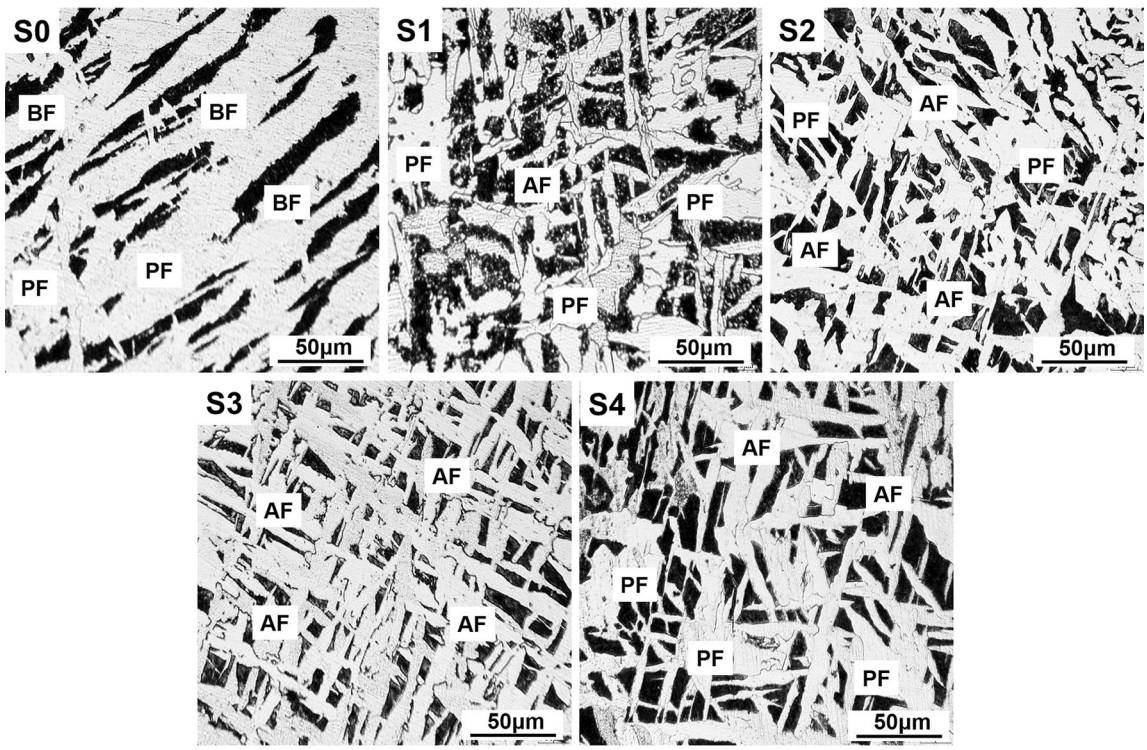

Fig. 8—Microstructure of billet samples with increasing additions of MgO nanoparticles.

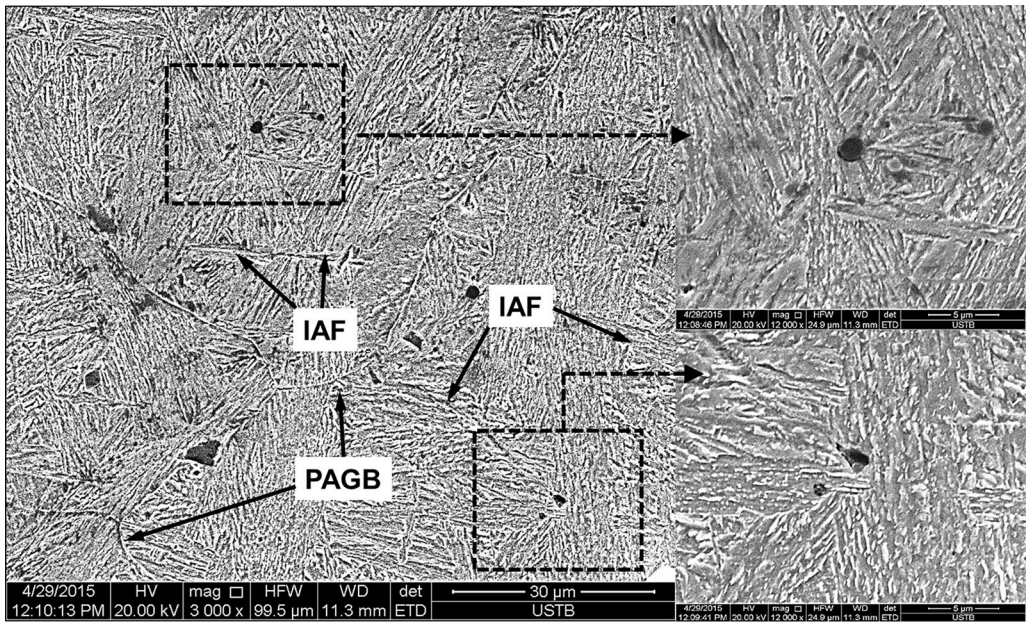

Fig. 9—Typical morphology of IAF induced by inclusions.

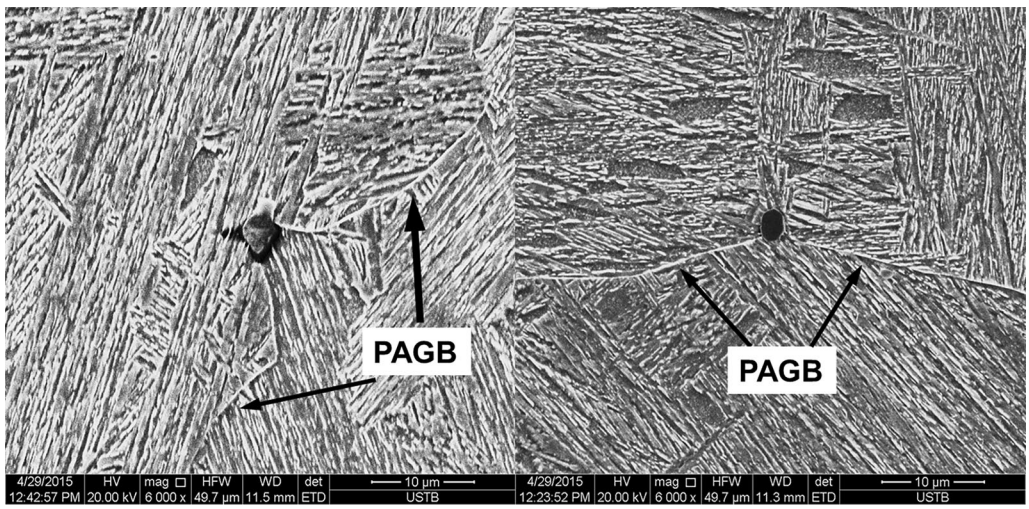

Fig. 10—Inclusions located on primary austenite grain boundaries (PAGB).

IV. MECHANISTIC ANALYSIS

The development of microstructure during solidification of steel with and without the addition of nanoparticles is illustrated schematically in Figure 12. As discussed in Section III, all of the inclusions that can induce AF are characterized by the presence of $MgO\text{-}Al_2O_3$.

A. *Inclusion Characteristics*

It is well known that MgO is a thermally stable inclusion in molten steel. When the MgO nanoparticles mixed with AlSi nanoparticles are added to the steel melt, they are quickly dispersed within the liquid steel. The Al and Si dissolve in the steel melt. Due to the strong deoxidizing power of Al, it combines with dissolved oxygen to generate Al_2O_3 inclusions. The strong stirring effect within the steel in the mold facilitates the formation of $MgO\text{-}Al_2O_3$ inclusions. As the steel temperature decreases, MnO precipitates and reacts with $MgO\text{-}Al_2O_3$ inclusions. When the liquid steel temperature decreases below the precipitation temperature of sulfides, MgS and MnS inclusions begin forming on the surface of the oxide inclusions. When these duplex inclusions are observed with the SEM, the oxide inclusions appear in dark color and the sulfide inclusions in light color.

As shown in Figure 7, the average size of inclusions increases with the increase in the amount of added nanoparticles. This is mainly due to the different sizes of particles which can act as the precipitation cores for other inclusions. With increase in the number of

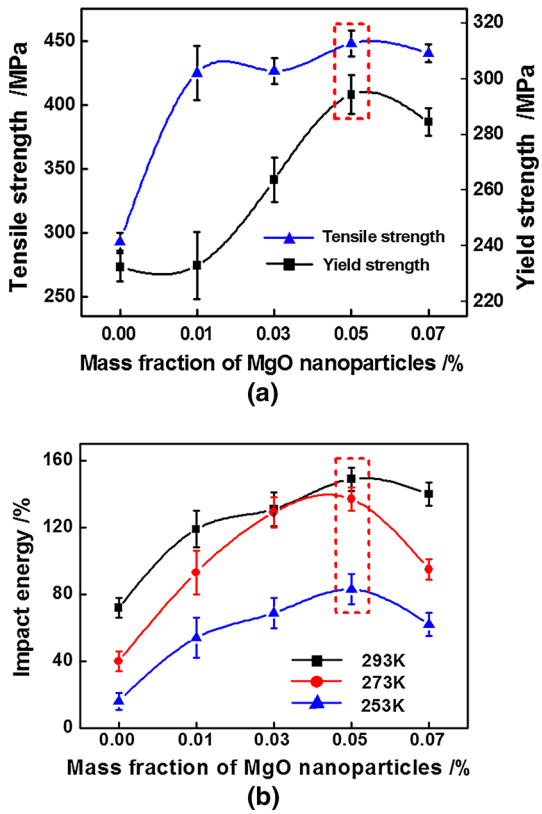

Fig. 11—Mechanical properties of steels with different additions of MgO nanoparticles.

nanoparticles in the steel melt, the space between adjacent particles decreases and the probability of collision between adjacent particles will increase. This ultimately results in the aggregation and growth of particles acting as the precipitation cores for other inclusions. The precipitation of sulfide reaction products on the surface of oxide inclusions further increases the inclusion size.

B. *Pinning Effect*

Since the inclusions in S0 steel as shown in Figure 4 apparently do not serve as nucleation cores for inducing IAF, nor do they retard the growth of austenite grains, the influence of these kinds of inclusions on the development of microstructure can be ignored. Figure 12(A) shows a schematic of the microstructural changes that take place during solidification of S0 steel. When the temperature decreases below the liquidus temperature, primary austenite grains start nucleating and growing as described in the second step of Figure 12(A). The main factors affecting grain size in steel without added nanoparticles are heat treatment conditions and steel composition, especially trace amounts of alloying elements. However, in steel with added nanoparticles, many fine inclusions can act as pinning particles to retard the growth of austenite grains as shown in the second step of Figure 12(B). Ultimately, as shown in the third step in Figure 12, the average size of austenite grains in the latter case is smaller than that in the former.

Inclusion size is the predominant factor that determines whether or not a particular inclusion will cause a pinning effect. This can be explained with the aid of Zener's theory[34] that the driving force for grain growth due to curvature of the grain boundary can be counteracted by a pinning (drag) effect exerted by particles located at the boundary. The pinning effect can be described in terms of the following equation:

$$R = \frac{3}{4} \cdot {}^{r}\!/_{f} \qquad [1]$$

where R is the Zener limit, r the radius of the pinning particles, and f the volume fraction of particles. The parameter f can be calculated from Eq. [2]:

$$f = \frac{\pi}{6} \cdot N_V r^3, \qquad [2]$$

where N_V is the quantity of inclusions per unit volume.

According to the above equations, it can be deduced that by appropriately increasing the inclusion size, the probability that it will serve as an effective pinning particle is increased. Also increasing the number density of inclusions will raise the effective quantity of pinning particles. If the inclusion size is excessively large, it may also cause billet defects. If the inclusion size is too small, the austenite boundary would simply pass over these inclusions until it meets pinning particles of appropriate size, or collides with other austenite boundaries in the process of grain growth. As represented in the third step in Figure 12(B), some inclusions locate on the primary austenite boundary and others reside within the primary austenite.

C. *Ferrite Nucleation*

The main factors that determine whether or not inclusions can act as nucleation cores to induce the generation of IAF are inclusion type and inclusion size. Different kinds of inclusions have a different inducing ability for AF, which is mainly related to the value of the contact angle θ between ferrites and inclusions. Generally, different kinds of inclusions have different contact angles. When two types of inclusions have similar size, the one with a relatively small contact angle would have the greater ability to induce AF. Based on nucleation dynamics, Christian and Wang *et al.*[35,36] have developed a method for calculating the rate of ferrite nucleation on the surface of an inclusion. The ferrite nucleation rate is a parameter that quantifies the degree of difficulty associated with nucleation. The greater the ferrite nucleation rate, the easier it is for ferrite to nucleate on the surface of an inclusion. Figure 13 shows the variation in the ferrite nucleation rate as a function of the inclusion size (R^*) for a contact angle θ of $\pi/3$. R^* is a non-dimensional parameter defined by the expression:

$$R* = R_I / r_C \qquad [3]$$

R_I represents the radius of curvature of the inclusions and r_c is the critical radius of inclusions that will nucleate ferrite.

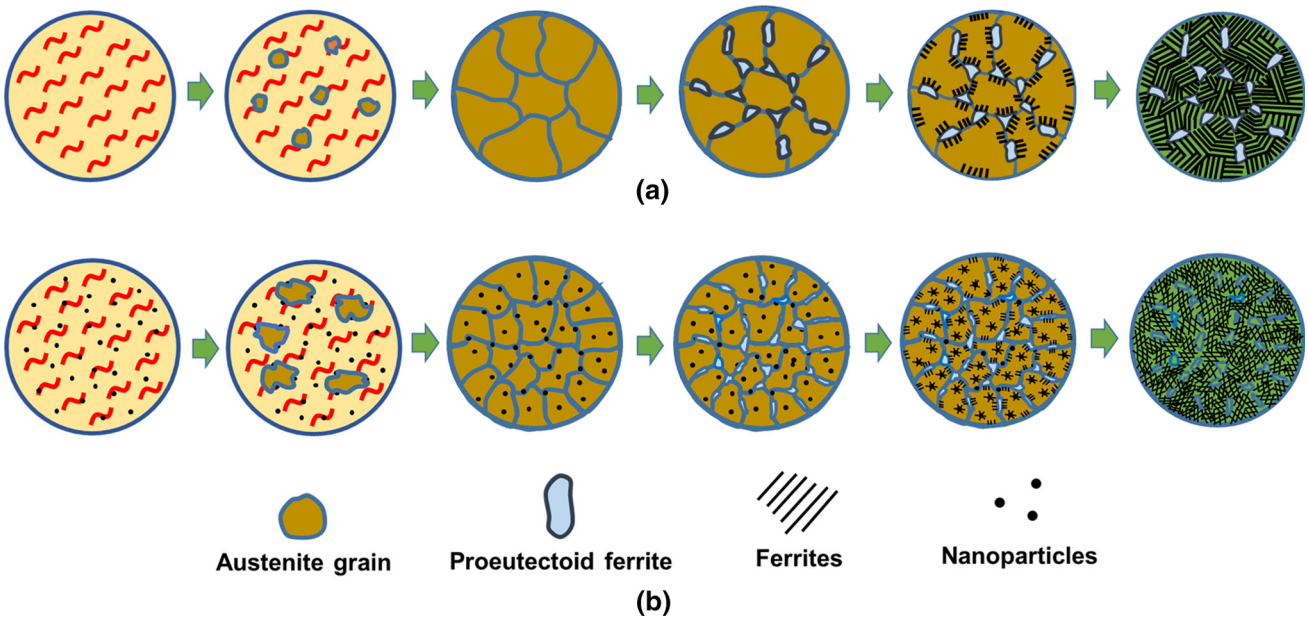

Fig. 12—Schematic diagram of microstructure evolution during solidification of steel. *A* Without addition of nanoparticles; *B* With addition of nanoparticles.

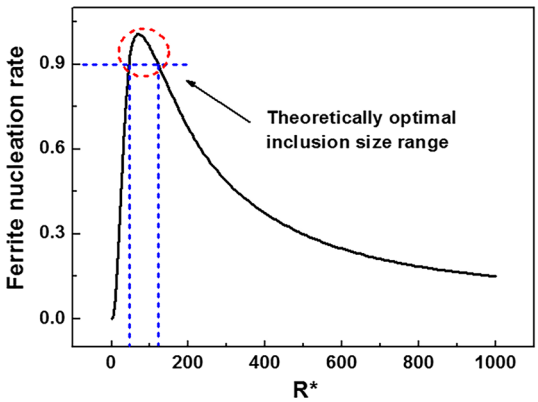

Fig. 13—Relationship between ferrite nucleation rate and inclusion size.

It can be deduced that when the contact angle θ is $\pi/3$, there exists a special range for inclusion size as indicated by the red loop in Figure 13 and only within this range, do the inclusions have a relatively large ferrite nucleation rate. It can be inferred that $MgO\text{-}Al_2O_3$-bearing inclusions have a similar tendency and when the inclusion size exceeds a certain value, the ability of inclusions to induce AF formation will greatly decline. This explains why after the average size of inclusions increased to 3.5 μm, the proportion of AF in the microstructure was lower than that found for the optimum formation of AF when the average inclusion size was 1.8 μm. It also explains the observation that the average size of inclusions that function as pinning particles is larger than that of inclusions that serve as nucleation cores for inducing AF.

When the steel temperature decreases below the γ–α phase transformation temperature, the proeutectoid ferrites first form along austenite grain boundaries. These ferrites generally consist of a coarse banded structure as depicted in the fourth step of Figure 12(A). However, since the grain size of austenite in steel with added nanoparticles is relatively small, the size of proeutectoid ferrites is also smaller as shown in the fourth step in Figure 12(B). Subsequently, other types of ferrites also form. Generally, AF would grow perpendicular to the grain boundaries of proeutectoid ferrite or austenite. In steel containing nanoparticles, in addition to the mechanisms mentioned above, ferrites also form on the surface of $MgO\text{-}Al_2O_3$-bearing inclusions as represented by the fifth step in Figure 12(B). In such steels, the microstructure is finer and the degree of AF interlocking is higher, both of which ultimately result in improved mechanical properties as shown in Figure 11.

V. SUMMARY AND CONCLUSION

Adding second phase nanoparticles to molten steel within the mold in the vicinity of the submerged nozzle outlet ensures the particles are well dispersed within the continuously cast billet. After adding MgO nanoparticles pre-dispersed with AlSi alloy nanoparticles to HPB300 steel, the majority of the reaction products were $MgO\text{-}Al_2O_3$-bearing inclusions. With the mass fraction of nanoparticles increasing from 0.01 to 0.03 pct, 0.05 and 0.07 pct, the average size of inclusions was 1.0, 1.2, 1.8, and 3.5 μm, respectively. These inclusions were significantly smaller than those found in steel without addition of MgO nanoparticles, where the average inclusion size was 7.0 μm.

The majority of the $MgO\text{-}Al_2O_3$-bearing inclusions have a good ability for inducing AF formation. As the mass fraction of nanoparticles increased from 0.01 to 0.05 pct, the proportion of AF in the microstructure

progressively increased. When the mass fraction of nanoparticles reached 0.07 pct, the ability of inclusions to induce AF formation, greatly declined and the proportion of AF was also diminished. This is mainly attributed to the value of the ferrite nucleation rate which is relatively high only within a small range of inclusion sizes. The test results from this plant study confirm that when the inclusion size is sufficiently large, these inclusions can function as pinning particles.

When the mass fraction of MgO nanoparticles is 0.05 pct, the degree of interlocking of AF within the microstructure of billet specimens is optimized and this is associated with peak values for mechanical properties, specifically yield strength, tensile strength, and impact energy.

ACKNOWLEDGMENTS

This research is supported by the National Science Foundation of China (No. 51474076 and 51304016) and open fund of State Key Laboratory of Advanced Metallurgy (No.KF14-02 and KF14-06). Appreciation is also expressed to the Natural Sciences and Engineering Research Council of Canada for support of steel-related research at the University of Toronto.

NOMENCLATURE

AF	Acicular ferrite
BF	Banded ferrite
EAM	External addition method
EDS	Energy-dispersive spectrometry
f	Volume fraction of particles
IAF	Intragranular acicular ferrite
IPM	Internal precipitation method
N_V	Quantity of inclusions per unit volume
PAGB	Primary austenite grain boundaries
PF	Polygonal ferrite
r	Radius of the pinning particles
R	Zener limit
R^*	A non-dimensional parameter which is proportional to the radius of curvature of the inclusions
R_I	Radius of curvature of the inclusions
r_C	Critical radius of inclusions that will nucleate ferrite
SEM	Scanning electron microscopy
θ	Contact angle between ferrites and inclusions

REFERENCES

1. X. Zhang, L. Fan, Y. Xu, J. Li, X. Xiao, and L. Jiang: *Mater. Des.*, 2015, vol. 65, pp. 682–89.
2. C. Zhang, X. Song, P. Lu, and X. Hu: *Mater. Des.*, 2012, vol. 36, pp. 233–42.
3. J. Kobayashi, S.M. Song, and K.I. Sugimoto: *ISIJ Int.*, 2012, vol. 52, pp. 1124–29.
4. C.J. Martis, S.K. Putatunda, and J. Boileau: *Mater. Des.*, 2013, vol. 46, pp. 168–74.
5. D. Rasouli, S.K. Asl, A. Akbarzadeh, and G.H. Daneshi: *Mater. Des.*, 2009, vol. 30, pp. 2167–72.
6. M. Niikura, M. Fujioka, Y. Adachi, A. Matsukura, T. Yokota, Y. Shirota, and Y. Hagiwara: *J. Mater. Process. Technol.*, 2001, vol. 117, pp. 341–46.
7. P. Cizek, B. Wynne, C. Davies, B. Muddle, and P. Hodgson: *Metall. Mater. Trans. A*, 2002, vol. 33A, pp. 1331–49.
8. A. Kojima, Y. Watanabe, Y. Terada, A. Yoshie, and H. Tamehiro: *ISIJ Int.*, 1996, vol. 36, pp. 603–10.
9. H. Beladi, G.L. Kelly, A. Shokouhi, and P.D. Hodgson: *Mater. Sci. Eng. A-Struct.*, 2004, vol. 371, pp. 343–52.
10. P.C.M. Rodrigues, E.V. Pereloma, and D.B. Santos: *Matet. Sci. Eng. A-Struct.*, 2000, vol. 283, pp. 136–43.
11. C. Zener: *Trans. Am. Inst. Metall. Eng.*, 1949, vol. 175, pp. 15–17.
12. P.L. Harrison and R.A. Farrar: *J. Mater. Sci.*, 1981, vol. 16, pp. 2218–26.
13. J. Takamura and S. Mizoguchi: *Proceedings of 6th International Iron and Steel Congress.*, Iron and Steel Institution Japan, Tokyo, 1990, vol. 01, pp. 591–95.
14. S. Mizoguchi and J. Takamura: *Proceedings of 6th International Iron and Steel Congress.*, Iron and Steel Institution Japan, Tokyo, 1990, vol. 01, pp. 598–604.
15. H. Homma, S. Ohkita, S. Matsuda, and K. Yamamoto: *Weld J.*, 1987, vol. 66, pp. 301–09.
16. Y. Tomita, N. Saito, T. Tsuzuki, Y. Tokunaga, and K. Okamoto: *ISIJ Int.*, 1994, vol. 34, pp. 829–35.
17. K. Yamamoto, T. Hasegawa, and J. Takamura: *ISIJ Int.*, 1996, vol. 36, pp. 80–86.
18. J. Shim, Y.W. Chou, S.H. Chung, J.H. Shim, and D.N. Lee: *Acta Mater.*, 1999, vol. 47, pp. 2751–60.
19. J.S. Byun, J.H. Shim, Y.W. Chou, and D.N. Lee: *Acta Mater.*, 2003, vol. 51, pp. 1593–606.
20. S.H. Nedjad and A. Farzaneh: *Scr. Mater.*, 2007, vol. 57, pp. 937–40.
21. R.A. Ricks, P.R. Howell, and G.S. Barritte: *J. Mater. Sci.*, 1982, vol. 17, pp. 732–40.
22. S.S. Babu and S.A. David: *ISIJ Int.*, 2002, vol. 42, pp. 1344–53.
23. S. Talas and R.C. Cochrane: *J. Alloys Compd.*, 2005, vol. 396, pp. 224–27.
24. K. Nishioka and K. Ichikawa: *Sci. Technol. Adv. Mater.*, 2012, vol. 13, pp. 1–20.
25. M. Hasegawa and K. Takeshita: *Metall. Mater. Trans. B*, 1978, vol. 09B, pp. 383–88.
26. M. Hasegawa and K. Takeshita: *Tetsu-to-Hagané.*, 1976, vol. 62, pp. 201–09 (in Japanese).
27. M. Hasegawa and K. Takeshita: *Tetsu-to-Hagané.*, 1977, vol. 63, pp. 294–302 (in Japanese).
28. M. Hasegawa and K. Takeshita: *Bull. Jpn. Inst. Met.*, 1976, vol. 15, pp. 462–64 (in Japanese).
29. J.M. Gregg and H.K.D.H. Bhadeshia: *Acta Mater.*, 1997, vol. 45, pp. 739–48.
30. G.C. Wang, T.M. Wang, S.N. Li, and K.M. Fang: *Chin. J. Eng.*, 2007, vol. 29, pp. 578–81 (in Chinese).
31. Z.D. Huang, J.P. Niu, Q.K. Cai, and L. Wang: *J. Northeast. Univ.*, 2009, vol. 30, pp. 997–1000 (in Chinese).
32. B. Wen and B. Song: *Steel Res. Int.*, 2012, vol. 83, pp. 487–95.
33. H.S. Kim, H.G. Lee, and K.S. Oh: *Met. Mater. Int.*, 2000, vol. 06, pp. 305–10.
34. C.S. Smith: *Trans. AIME*, 1948, vol. 175, pp. 15–51.
35. J.W. Christian: in *Physical Metallurgy*, 1 st ed., R.W. Cahn, ed., North-Holland Publishing Company, Amsterdam, 1977, pp. 479–580.
36. W. Wang and L.M. Fu: *Acta Metall. Sin.*, 2008, vol. 44, pp. 723–28 (in Chinese).